Electronic supplementary information for Bubbles and drops between circular frames: Shape, force and stability analysis

F. Walzel[1]*, J. Dijoux[1], L. Jacomine[1], E. Harle[1], P. Muller[1], T. Charitat[1]†, and W. Drenckhan[1]

[1]UPR 22/CNRS, Institut Charles Sadron, Université de Strasbourg,
23 rue du Loess, BP 84047 67034 Strasbourg Cedex 2, France

August 22, 2024

Contents

*Address for correspondence, friedrich.walzel@ics-cnrs.unistra.fr
†Address for correspondence, thierry.charitat@ics-cnrs.unistra.fr

S1 Experimental details

S1.1 Pinned interfaces

From a mathematical point of view, pinned bubbles are surfaces where some points on the surface are fixed points in space. Here the fixed points are on circular frames. The following explains how the pinning was realised in our experiments. We deal with static interfaces controlled by interfacial tension. That means the only forces exerted on the contact line between the frame and the interface are interfacial tensions. The force equilibrium at the contact line in the frame plane in radial direction is expressed with the Young-Dupré law [1]

$$\gamma_{\mathrm{Fi}} - \gamma_{\mathrm{Fo}} = \gamma_{\mathrm{b}} \cos\theta, \tag{S1}$$

illustrated in Fig. S1a. The interfacial tension between the frame and the inner fluid is γ_{Fi}. The interfacial tension between the frame and the outer fluid is γ_{Fo}. The interfacial tension between the inner and outer fluid is γ_{b}. Since in most cases all three interfacial tensions are constant, the angle θ at the contact line is constant as well. If the volume or other constraints change, the contact line between the frame surface and the bubble interface can move to adapt to the new constraints. Here we want to work with pinned interfaces. This is achieved, when one of the three interfacial tensions on the contact line is variable in amplitude or the surface has a kink. Discontinuities in geometry could be seen as an infinitely strong gradient in space for the interfacial tension, as sketched in Fig. S1b. To move the contact line over the edge of the frame the angle θ between the surface and the horizontal plane is free to take any value between $\theta_{1\mathrm{g}}$ and $\theta_{2\mathrm{g}}$ ("g" for geometrical discontinuity). We therefore define the pinning strength

$$\Delta\theta = \theta_{1\mathrm{g}} - \theta_{2\mathrm{g}}. \tag{S2}$$

The maximal $\Delta\theta$ for a geometrical discontinuity is therefore 180°. We have almost achieved this with very thin edges of the frames (Fig. S1c left and right frame). In general, the frames have $90° < \Delta\theta < 180°$.

For soap films the scenario is slightly more complicated. The film will always form a meniscus at the contact to the pinning object. The geometry of the meniscus plays an important rule for the pinning strength. It is influenced by the energy and geometry of the surface also by the liquid fraction. A good approximation for the contact angle between an object and a soap film is $\theta = 90°$. It is exact for a soap film on a homogeneous plane.
For our experimental setup it was important that the change in θ during the tilting instability and a detachment instability was smaller than the $\Delta\theta$ defined by the setup. We used for that different frame geometries, see Fig. S1c. For some (R, V) we had to repeat the experiment with different frame geometries to measure the tilting instability and a detachment instability.

S1.2 Bond number

The Bond number is a dimensionless quantity measuring the importance of gravitational forces compared to interfacial tension forces.

In the case of drops, it is given by

$$\mathrm{Bo} = \left(\frac{h}{\lambda_{\mathrm{c}}}\right)^2 = \frac{\Delta\rho g h^2}{\gamma}, \tag{S3}$$

where h is the characteristic length in the vertical direction, and λ_c the capillary length ($\lambda_{\mathrm{c}} = \sqrt{\gamma/\Delta\rho g}$). For the silicone oil / water system one obtains $\mathrm{Bo} < 2.5 \cdot 10^{-3}$ (see Fig. S2).

For soap bubbles, the average film thickness e_0 must be taken into account (see for example the work of Cohen *et al.*[2]) leading to

$$\mathrm{Bo} = \left(\frac{\Delta\rho g e_0 h}{\gamma}\right)^2. \tag{S4}$$

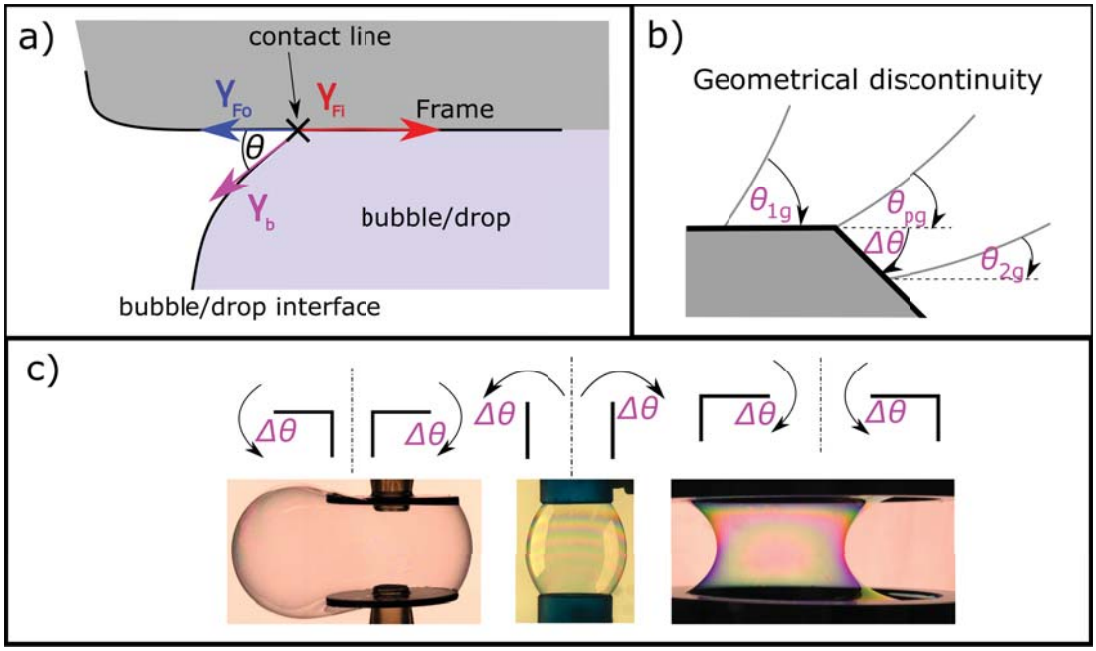

Figure S1: Three schemes explaining how the frame geometries are chosen. a) Force equilibrium between the different interfacial tensions at one point of the contact line between the bubble interface and the frame. γ_b is the interfacial tension between the outer and inner fluid, γ_{Fo} is the interfacial tension between the frame and the outer fluid and γ_{Fi} is the interfacial tension between the frame and the inner fluid. The contact point is part of the contact line between the frame surface and the bubble interface. b) Principal idea of pinning with help of a geometrical discontinuity. The contact line is pinned for a contact angle θ_p between $\theta_{1\mathrm{g}} > \theta_p > \theta_{2\mathrm{g}}$ with $\Delta\theta = \theta_{1\mathrm{g}} - \theta_{2g}$, "g" stands for geometrical discontinuity. c) Chosen frame geometries for different boundary conditions, $\hat{h}$, $\hat{R}$ and θ_{c}.

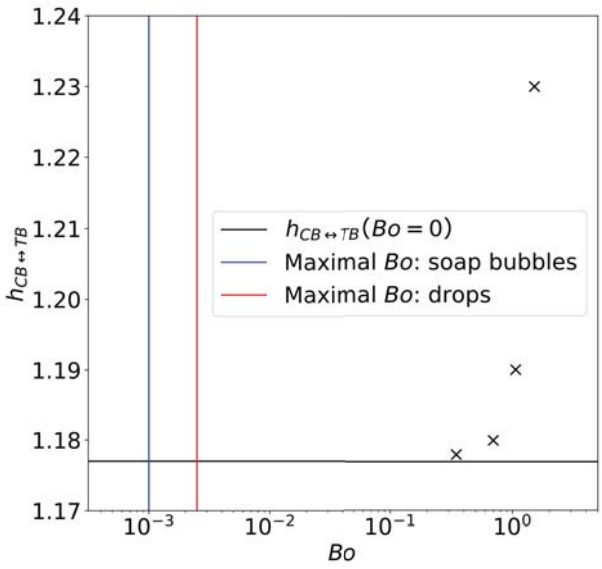

Figure S2: Influence of gravity (expressed by the Bond number Bo) on the transition height $h_{CB\longleftrightarrow TB}$ of the tilt instability for the case $\theta_c = 0°$ and $\hat{R} = 0.7$. The results are obtained with Surface Evolver. The maximal Bo encountered in the experiments for the two used systems, soap bubbles and water drops with SDS in silicone, are highlighted in blue and red, respectively. The horizontal line shows $h_{\mathrm{CB}\leftrightarrow\mathrm{TB}}$ for $\mathrm{Bo} = 0$.

In our experiments, with an estimated film thickness of 1 µm, $\mathrm{Bo} < 10^{-3}$.

In both cases we obtain very small Bo and gravity is therefore negligible. The assumption of a constant Δp is therefore reasonable.

In order to estimate the influence of gravity for the range of Bo numbers used in our experiments, we show in Figure S2 how the onset of the tilting instability $h_{CB\leftrightarrow TB}$ is expected to depend on Bo for the case $\theta_c = 0°$ and $\hat{R} = 0.7$. These results are obtained by Surface Evolver simulations. It can be seen that for soap bubbles and water drops in silicone, the influence of gravity is negligible in the range of Bo of our experiments.

S1.3 Pressure measurement

Fig. S3 shows the two pressure sensors for the upper and bottom bubble (drop) with the important parameters which are needed to obtain the pressure difference between the inside and outside of the two bubbles (drops). Since it is impossible to place the pressure sensor directly at the interface of the bubbles (drops) there is always a distance in space between the point where we measure the pressure difference and the point where we want to know the pressure difference. In the general case these two pressures are not the same due to hydrostatic and hydrodynamic pressures. In the absence of liquid flow, the differences in pressure between the sensors and the drop interfaces are only related to hydrostatic pressures. We will start with this simple case. Afterwards, we will show that for the applied flow rates we can also neglect hydrodynamic effects.

The pressure difference between the inside and outside of the lower bubble (drop) is

$$\Delta p_A^- = 2H_A^-\gamma_b^- = p_i^- - p_o = p_S^- + (L^- - L_A^-)\rho_i g - \rho_o g(L_F^- - L_A^-), \tag{S5}$$

where the index "$-$" stands for "bottom", "i" for "inside", "o" for "outside", "A" for "Apex", "F" for frame, and "b" for "bubble". p_S^- is the pressure measured at the sensor for the bottom bubble and Δp_A^-

the pressure jump across the bottom bubble interface at the apex. The distances L are illustrated in Fig. S3. The pressure jump at the apex is the Laplace pressure at the apex. It is proportional to the mean curvature at the apex H_A^- and the interfacial tension of the bottom bubble (drop) γ_b^-. Due to the axisymmetric shape of the bubbles the two principle curvatures at the apex are identical. That is why we took the apex as our calibration point. The two densities of the inner and outer phase, ρ_i and ρ_o, are measured independently with Mettler Toledo D4 at 20 $°C$. By rearranging eqn. (S5) we obtain

$$p_S^- + gL_A^-(\rho_o - \rho_i) = 2H_A^-\gamma_b^- + \rho_o g L_F^- - \rho_i g L_- = 2H_A^-\gamma_b^- + K^-, \tag{S6}$$

with $K^- = \rho_o g L_F^- - \rho_i g L^-$. Since the temperature, the bottom frame position and the liquid level of the outer liquid are constant, K^- is constant as well. The liquid level stays constant since the temperature is constant and evaporation of the the outer liquid is avoided. For the calibration of the pressure sensor the two liquid phases are chosen in a manner that γ_b^- is constant as well (high concentration of low molecular weight surfactants). In this case, one can make a linear fit between the measured H_A^- and p_S^- for quasi-static inflation and deflation of the bubble. The measured pressure of the sensor has to be corrected with $gL_A^-(\rho_o - \rho_i)$ where only L_A^- changes during the experiment and is measured optically during the calibration with a precision of 10 μm. The same procedure is applied for the upper sensor S^+. To obtain the respective equations one has to replace only the index "$-$" with "$+$" and change the sign in front of L_A^- in (S6) to obtain

$$p_S^+ - gL_A^+(\rho_o - \rho_i) = 2H_A^+\gamma_b + \rho_o g L_F^+ - \rho_i g L^+ = 2H_A^+\gamma_b + K^+, \tag{S7}$$

with $K^+ = \rho_o g L_F^+ - \rho_i g L^+$. Since the upper frame changes position during an experiment, K^+ changes as well. That is why we relate the variable K^+ to the frame distance between the bottom and top frames L_{FF} which is also measured optically. It follows

$$K^+ = K_0^+ + g(L_{FF0} - L_{FF})(\rho_o - \rho_i), \tag{S8}$$

where the index "0" indicates the values at the onset of the experiment. The variables K_0^+ and L_{FF0} are constants and obtained during the pressure calibration of the upper bubble. Consequently the calibration constant K^+ is a function of L_{FF}. Whenever possible, the calibration is repeated before and after a set of experiments to verify that the calibration constants do not change with time. Fig. S4 shows an example of a typical pressure calibration inflation/deflation curve. On the left part in Fig. S4 the measured pressure (corrected with the changing bubble height L_A^-) is plotted against H_A^-. The color of the measurements symbolise the time: starting from purple at t_0, it passes through green at t_1, before ending at yellow at t_2. The red line is the obtained calibration curve, which gives K^- and γ_b. The right part of Fig. S4 compares Δp_A^- obtained from image analysis with the Young-Laplace equation and the pressure sensor for the inflation and deflation. Both show excellent agreement. Since for inflation and deflation the same pressures were measured for the same mean curvatures (Fig. S4), we can conclude that the hydrodynamic effects are negligible for the applied flow rates.
Fig. S5 shows examples of the physically measured pressures (right) and forces (left) for different $\hat{R}$ for typical withdrawing/approaching experiments.

S2 Delaunay Surfaces

S2.1 Parametrisation of Delaunay Surfaces

The five different axisymmetric constant mean curvature surfaces (nodoid, sphere, unduloid, cylinder and catenoid) can be obtained by rolling a cone section (Fig. S6) along the symmetry axis of the Delaunay surfaces and following one of the focal points of the cone sections. The path of the focal point than draws a section in the rz-plane of the surface.
The parametrisation of an **unduloid** is obtained by rolling an ellipse along the symmetry axis. One

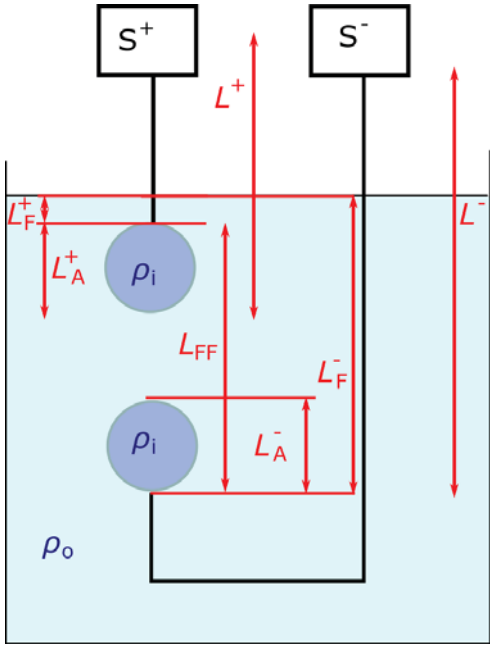

Figure S3: Scheme showing the relationship between the measured pressures in the Sensors S (Fig. 5 (10)) and the pressure difference between the inside and the outside of the bubbles. L are lengths, ρ densities and p pressures. The indices "+" and "-" stand for "top" and "bottom" respectively, "i" and "o" for "inside" and "outside", "A" for "apex" and "F" for "frame".

obtains

$$\begin{aligned} \tilde{z}(\omega) &= -2\tilde{F}_z \int_{\omega_0}^{\omega} \frac{du}{(1+e\cos u)\sqrt{1-e^2\cos^2 u}}, \\ \tilde{r}(\omega) &= \sqrt{-\tilde{F}_z \frac{1-e\cos\omega}{1+e\cos\omega}}, \end{aligned} \tag{S9}$$

with $e = \sqrt{4\tilde{F}_z + 1}$ being the eccentricity of the ellipse and u and ω the angular position of the rolling ellipse above the plane, with ω_0 the starting point of the surface and ω the current point.
The limit case of a **cylinder** is obtained when $e = 0$ with $\tilde{F}_z = -0.25$. Eqn.s (S9) then become

$$\begin{aligned} \tilde{z}(\omega) &= -2\tilde{F}_z \int_{\omega_0}^{\omega} du, \\ \tilde{r}(\omega) &= \sqrt{-\tilde{F}_z} = \frac{1}{2}. \end{aligned} \tag{S10}$$

The parametrisation of a **nodoid** is obtained by rolling a hyperbola along the symmetry axis of the nodoid and following one of the focal points. One obtains [3]

$$\begin{aligned} \tilde{z}(\omega) &= -2\tilde{F}_z \int_{\omega_0}^{\omega} \frac{\cos u du}{(e+\cos u)\sqrt{e^2-\cos^2 u}}, \\ \tilde{r}(\omega) &= \sqrt{-\tilde{F}_z \frac{e-\cos\omega}{e+\cos\omega}}. \end{aligned} \tag{S11}$$

The eccentricity e is a function of $\tilde{F}_z$ only. Consequently, $\tilde{F}_z$ defines the eccentricity of a conic section. The mean curvature H scales the size of the conic section, and $\tilde{F}_z$ changes the angle of the cutting plane

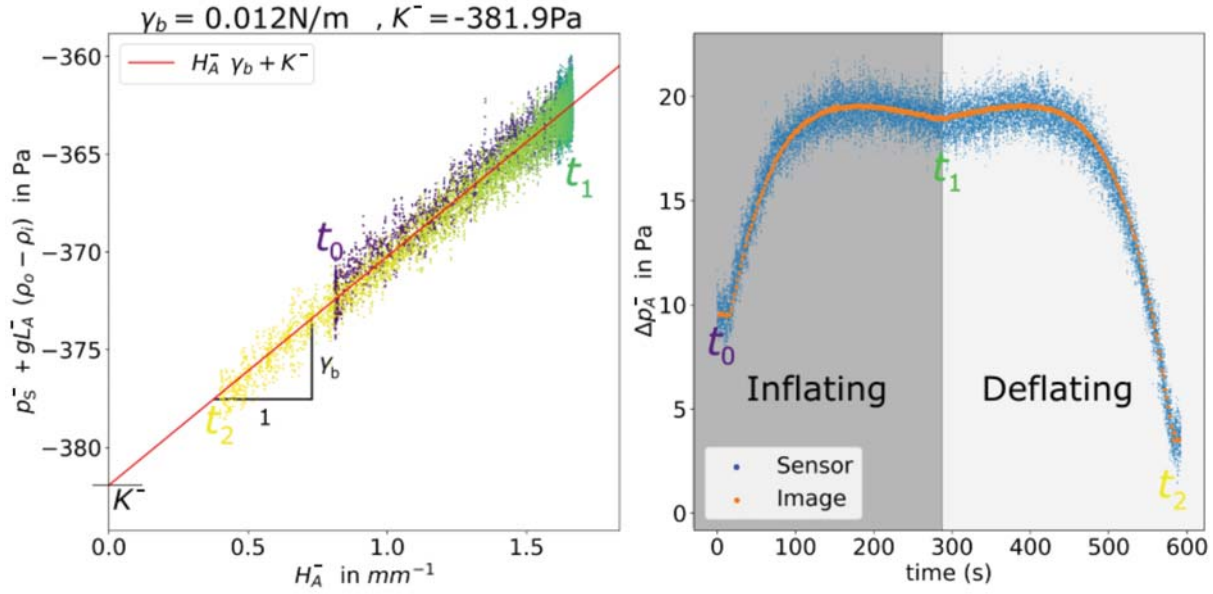

Figure S4: Left: measured pressure of the bottom bubble (drop) corrected with the apex height L_A^- plotted against the measured mean curvature at the bottom bubble apex H_A^- to obtain the calibration constant K^- and the interfacial tension of the bottom bubble γ_b using eqn. S6. Right: pressure evolution at the apex of the bottom bubble obtained either with the pressure sensor or with image analysis, plotted during an inflation and deflation of a bubble/drop.

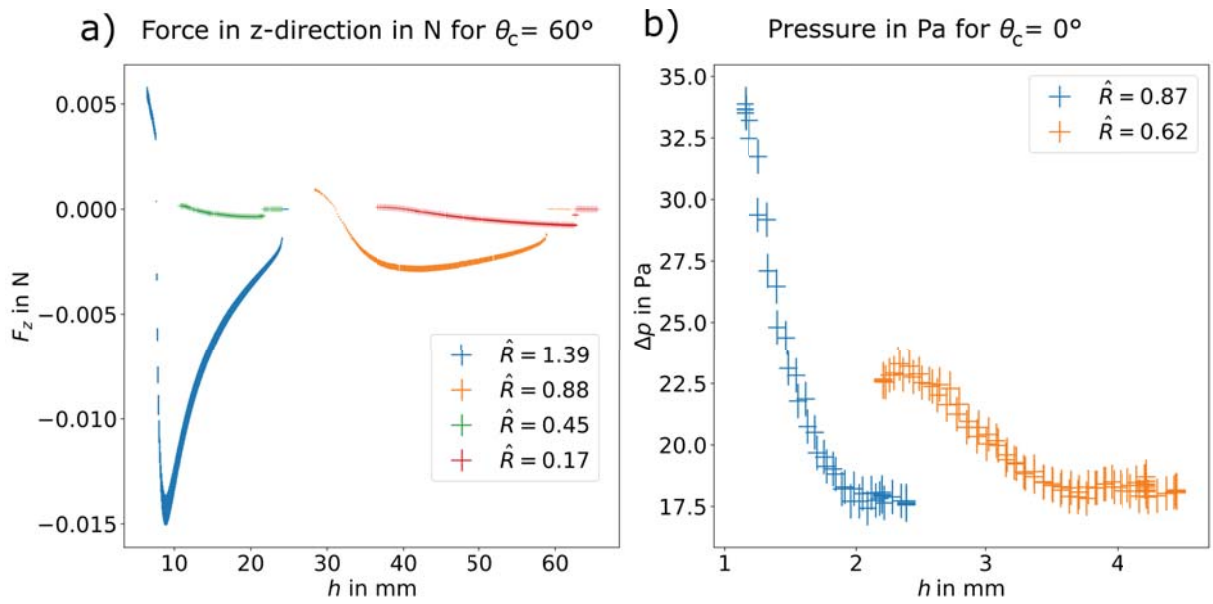

Figure S5: Left: normal force measurements for the double soap bubble setup for four different $\hat{R}$ values plotted over the physical distance between the frames. Right: pressure difference for two drops in contact for different $\hat{R}$.

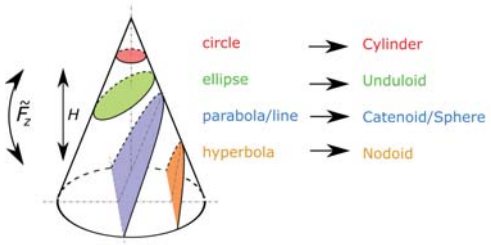

Figure S6: Examples of the different conic sections and the associated surfaces. $\tilde{F}_z$ rotates the cutting plane for the conic section and H shifts the cutting plane up or down. The figure is a modified figure from Wikipedia[4].

for the conic section. By increasing $\tilde{F}_z$, the plane becomes more vertical and by decreasing $\tilde{F}_z$ more horizontal. With $\tilde{F}_z = -0.25$, the plane is horizontal and cuts a circle out of the cone. H shifts the cutting plane with increasing H down and with decreasing H up, see Fig. S6.
If the tilt angle of the cutting plane is identical to the opening angle of the cone, then $e \to 1$ and $\tilde{F}_z \to 0$. One can distinguish two different cases. In the first case, $H \neq 0$ goes against a fixed value and we obtain a line as a conic section with a sphere as the associated surface. One obtains the unit **sphere**

$$\begin{aligned} \tilde{z}(\omega) &= \sin\omega, \\ \tilde{r}(\omega) &= \cos\omega, \end{aligned} \tag{S12}$$

with $-\pi/2 \geq \omega \geq \pi/2$ and $\tilde{F}_z = 0$. For the sphere we use the same parametrisation variable ω, even if it is not the rolling parameter of the conic section.
For $H = 0$, the conic section is a parabola with a **catenoid** as the associated surface. For the catenoid we can no longer use our dimensionless representation where we multiply by the mean curvature H because it is zero. Therefore, we show in this case the lengths in dimensional form

$$\begin{aligned} z &= a\,\mathrm{arsinh}(\omega), \\ r &= a\sqrt{1+\omega^2}, \end{aligned} \tag{S13}$$

with the neck radius $a = \lim_{H\to 0;\,\tilde{F}_z\to 0} \tilde{F}_z/H$. By eliminating ω in eqn.s (S13) we obtain the classical equation of a catenoid

$$r = a\cosh\left(\frac{z}{a}\right). \tag{S14}$$

All five types of surfaces are present in the double bubble experiments.

S2.2 Cutting and scaling of the Delaunay surfaces

The Delaunay Surfaces have to fulfil a set of conditions given by our experimental setup. The following equations are related to the boundary conditions, the volume constraint (eqn. (S15)), the frame radius (eqn. (S16)), the distance h between the frames (eqn. (S17)) and the contact angle θ_c between the two bubbles (eqn. (S18)).

$$
\begin{aligned}
V &= |H|^{-3}(\omega,\omega_0)\tilde{V}(\omega,\omega_0) \\
&= |H|^{-3}(\omega,\omega_0)\int_{\tilde{z}(\omega_0)}^{\tilde{z}(\omega)}\pi\tilde{r}^2 d\tilde{z}, && \text{(S15)} \\
R &= |H|^{-1}(\omega,\omega_0)\tilde{r}(\omega), && \text{(S16)} \\
\frac{h}{2} &= |H|^{-1}(\omega,\omega_0)\tilde{z}(\omega,\omega_0), && \text{(S17)} \\
\frac{dr(\omega_0)}{dz(\omega_0)} &= \frac{d\tilde{r}(\omega_0)}{d\tilde{z}(\omega_0)} = \cot(\theta_c). && \text{(S18)}
\end{aligned}
$$

Finding a suitable surface for a specific set of boundary conditions is difficult, and there is no unique solution. A more efficient method is to fix $\tilde{F}_z$ and search for all surfaces which fulfil all boundary conditions except of one, for example the volume constraint or the distance between the two frames. That is the principle idea of the algorithm detailed which we use in the article and which we detail below.

- **Step 1: setting the problem**

  We choose a parameter that changes during an experiment, such as h, V, R or θ. In our case, it is h, but the method is more general and can be applied to other cases.

- **Step 2: Accessible force range**

  We define a range of $\tilde{F}_z$ with $\tilde{F}_{z,min} \leq \tilde{F}_z \leq \tilde{F}_{z,max}$. $\tilde{F}_{z,min} = -0.25$, and we choose a realistic value for $\tilde{F}_{z,max}$, depending on the other boundary conditions and on the investigated problem.

- **Step 3: Setting the surface type**

  We choose a value $\tilde{F}_z \in \left[-0.25, \tilde{F}_{z,max}\right]$, allowing to calculate the eccentricity e, and the parametrisation $\tilde{r}$, $\tilde{z}$ and dr/dz. This step defines if the surface is part of a cylinder, unduloid, sphere or nodoid.

- **Step 4 : Setting the starting point ω_0**

  To ensure the contact angle condition, we solve eqn. (S18) giving all possible start points ω_0 for the given $\tilde{F}_z$ and θ_c. Depending on $\tilde{F}_z$ and θ_c there are zero, one or two solutions for eqn. (S18).

- **Step 5 : Setting the end point ω_1**

  For each starting point ω_0 we have to ensure now the pressure difference (mean curvature) conditions. Calculating $H(\omega)$ with

  $$H(\omega)^{-1} = \sqrt[3]{\frac{V}{\tilde{V}(\omega)}} \qquad \text{(S19)}$$

  obtained with eqn. (S15), gives us the end point $\omega = \omega_1$ which solves eqn. (S16). This gives us the full profile which we compare to a profile obtained by experiments in Fig. S7.

- **Step 6: removing unphysical solutions**

  Solutions defined by the values of $\omega_0, H(\omega_1)$, and $\tilde{r}(\omega)$ are the Delaunay Surfaces which fulfil all the boundary conditions except the one chosen at Step 1 (in our case the distance between the two frames h). We now have to remove unphysical solutions.

  First, It makes sense to consider only the solutions which include not more than one period, since they are physically unstable [5, 6]. We therefore eliminate all solutions with $\pi \geq |\omega_0 - \omega_1|$.
  It is still possible to obtain several solutions, but in general only one corresponds to an energy minimum. Looking at the whole set of solutions which differ only in the height $\tilde{h}$, one can distinguish different branches and bifurcations in the h-F_z plane. To decide which branches are stable or

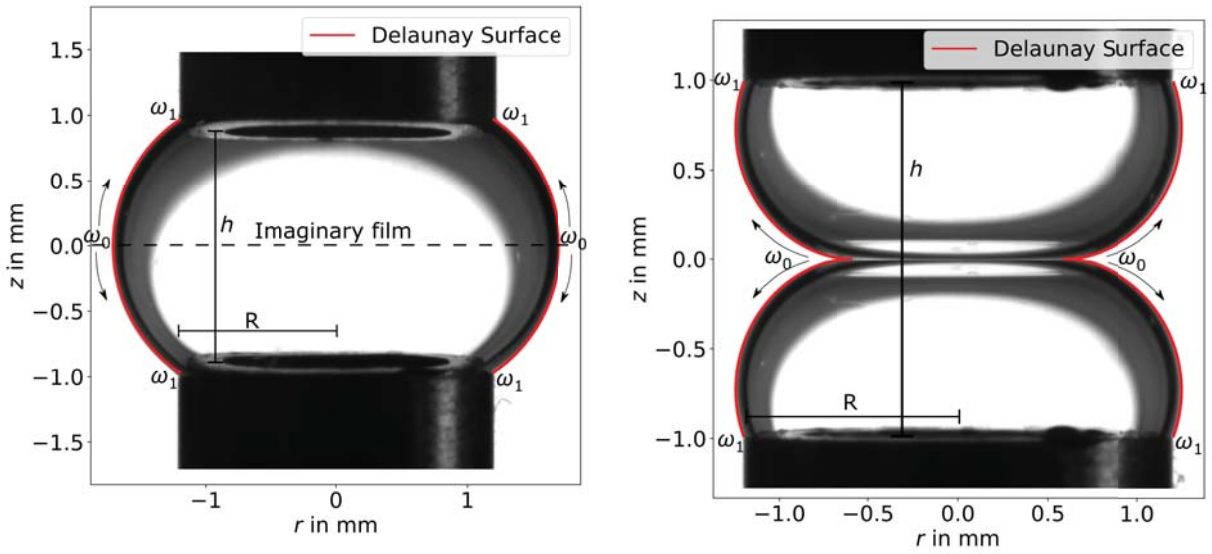

Figure S7: Comparison between the theoretical and experimental profile of a nodoid with $\tilde{F}_z = 0.25$ and $\theta_c = 90°$ on the left and $\tilde{F}_z = 0.34$ and $\theta_c = 0°$ on the right. The parameters ω_0, ω_1, R and h are also indicated.

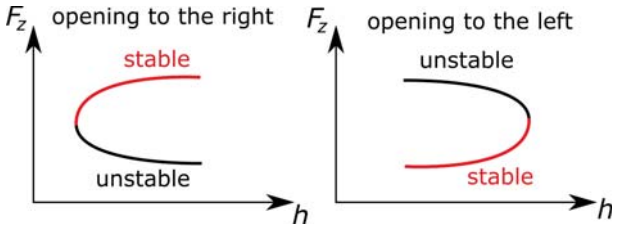

Figure S8: A fold with an opening to the right on the left and a fold with an opening to left on the right for a $F_z(h)$ curve [7].

unstable we use the second derivative of the surface energy $\underline{H}$, i.e., the Hessian matrix. If one eigenvalue of the Hessian matrix is negative the surface is unstable. To calculate this matrix analytically is most of the time impossible. But we know from the publication of J. H. Maddocks [7], that any fold in the h-F_z plane of curves representing extremal surfaces, must have a change of sign of at least one eigenvalue of $\underline{H}$. If the opening of the fold is to the left (Fig. S8) the upper branch is unstable. One eigenvalue of $\underline{H}$ becomes negative. Consequently, we can exclude all upper branches after a fold with the opening to the left systematically. Nevertheless, we cannot say that the lower branch is stable in all cases. To be 100% sure, we performed a simulation with Surface evolver.

Two examples of surfaces obtained with this procedure are in shown in Fig. S7 on the left a capillary bridge with $\theta_c = 90°$ and $\tilde{F}_z > 0$ and on the right for two drops in contact with $\theta_c = 0°$ and $\tilde{F}_z > 0$.

S3 Bubble frame detachment CB→DB, bubble bubble detachment CB→SB and their intersections for different θ_c

In this section we present detailed information on the exact location of the bubble frame detachment CB→DB and its intersection with the bubble bubble detachment CB→SB in the θ_c-$\hat{h}$-$\hat{R}$ space.
Fig. S9 gives with the sub-figures a, b, c, d and e an overview about the shapes and the position in the shape diagrams of CB→DB, CB→SB and the triple point Tr_1 of CB, SB and DB for different θ_c. Fig. S9a and b show the upper (dashed lines) and lower branches (solid lines) for CB→DB and the beginning of CB→SB (dashed dotted lines) with the intersection of CB→DB and CB→SB, the triple point Tr_1. Different colors represent different θ_c. Some examples of shapes on CB→DB for different θ_c are represented in Fig. S9d. For all of their shapes $\hat{r}_{,\hat{z}}(\pm\hat{h}/2) = 0$ (indicated in Fig. S9c with the right angle), and the total surface of both bubbles includes at least one complete period of a Delaunay surface. It follows that

$$\omega_1 = \pi \tag{S20}$$

$$|\omega_1 - \omega_0| > \pi. \tag{S21}$$

As discussed in Section 3.3, the upper branch (Fig. S9a blue dashed line) for CB→DB with $\theta_c = 90°$ has a maximum in $\hat{r}(\omega_1)$ and a minimum at $\hat{r}(\omega_0)$, the lower branch (Fig. S9a blue solid line) has a minimum at $\hat{r}(\omega_1)$ and a maximum at $\hat{r}(\omega_0)$. In order to have a $\theta_c < 90°$, $\hat{r}$ must increase with changing $\hat{z}$ at least in the close neighbourhood to $\hat{z} = 0$. Consequently, ω_0 moves away from the maxima and minima in $\hat{r}$ with decreasing θ_c. In order to fulfill the condition of eqn. (S20) and the condition of eqn. (S21), the upper branch is folded to larger $\hat{h}$ and smaller $\hat{r}$ for $\theta_c < 90°$ (Fig. S9a). As θ_c decreases, the upper and lower branches approach each other and become shorter (Fig. S9a).
One observes that Tr_1 is within the precision of the calculation on the point, where the upper and lower branch meet each other. The shapes related to this intersection have a $\tilde{F}_z(\theta_{min} = \theta_c)$ from Fig. 7 and fulfill eqn.s (S20) and (S21). They are unique shapes for a specific contact angle θ_c. An exception is the case of a capillary bridge. The triple point is not at the intersection of the upper and lower branches. It is inside of the upper branch. The part of the upper branch above Tr_1 is part of the unstable branch of a typical withdrawing/approaching experiment, see, for example, Fig. 9c and d.
Furthermore, a region in the phase diagrams in Fig. S9a and b close to Tr_1 with $\theta_c < 90°$ (shaded area in Fig. S9b) is not accessible for a typical withdrawing/approaching experiment. The size of this region decreases dramatically with a decreasing θ_c. To quantify this decrease, we calculated the relative difference between the coordinates ($\hat{R}$, $\hat{h}$) of the maximum in $\hat{R}$ and Tr_1 and plot it against θ_c in Fig. S9c. $\Delta\hat{R}/\hat{R}_{Tr_1}$ and $\Delta\hat{h}/\hat{h}_{Tr_1}$ decrease exponentially with decreasing θ_c. Numerical and experimentally we did not succeed to verify without doubt the stability in the shaded region in Fig. S9b. In the experiments ($\theta_c = 60°$), this region is already very small, below our measurement precision. In the simulations, the converging process turned out to be difficult for these shapes. The energy difference between stable shapes and unstable shapes is very small in this region. This makes it necessary to use a high number of facets to be able to distinguish between them. Therefore, the shapes need a lot of calculation time to converge towards a minimum. A complex convergence study is needed to solve the problem with certainty, which remains to be done. It therefore remains an interesting open question, if the shaded region in Fig. S9b belongs to stable or unstable shapes.
For $\theta_c = 0°$ the CB→DB does not exist, since there are never attractive forces between the bubbles. Consequently there are no unduloids fulfilling all boundary conditions. The upper and lower branch vanish in the triple point $Tr_1(\theta_c = 0°)$, which corresponds to the shape of two spheres in contact in a point.

S4 Catenoid

Since the normalised force $\tilde{F}_z$ is not defined for the catenoid (because $H = 0$) (see Section S2.1), we obtain the corresponding shapes separately from the other Delaunay surfaces. We take the parameterisation of

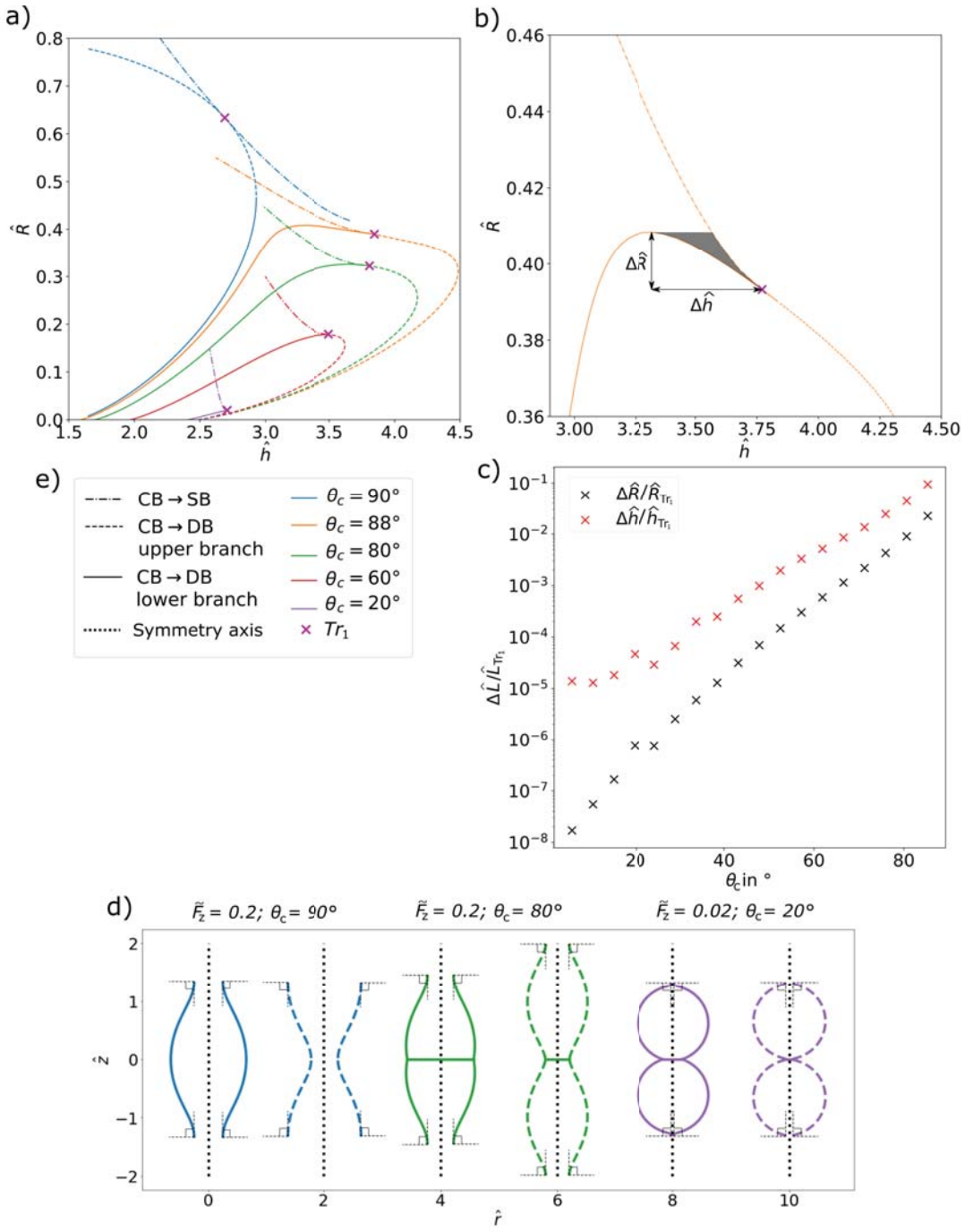

Figure S9: a) Lines and points in the phase diagram $\hat{R}$ over $\hat{h}$ for different θ_c, such as the $\hat{R}(\hat{h})$ for CB→SB and CB→DB, where the latter has been split into an upper and lower branch. The intersection of CB→SB and CB→DB (Tr_1) is also shown. b) A zoom in to the triple point Tr_1 for $\theta_c = 88°$ with the definition of $\Delta\hat{R}$ and $\Delta\hat{h}$. c) The evolution of $\Delta\hat{R}/\hat{R}_{\mathrm{Tr}_1}$ and $\Delta\hat{h}/\hat{h}_{\mathrm{Tr}_1}$ with increasing θ_c. d) Shapes with different θ_c and $\tilde{F}_z$, which fulfill the conditions of eqn.s (S20) and (S21) shifted horizontally for a better visualisation. e) The legend for all sub figures.

a catenoid (eqn. (S14)) and the derivative with respect to z

$$r_{,z} = \sinh\left(\frac{z}{a}\right). \tag{S22}$$

The standard catenoid is obtained with $\theta_c = 90°$ (top Fig. S10a). With $\theta_c < 90°$, a "diabolo" catenoid [8] is obtained (Fig. S10a). We are interested in the smallest $\hat{R}$ for a specific contact angle θ_c, which has a solution with $\Delta\hat{p} = 0$. For larger $\hat{R}$ there are always two solutions. For larger $\hat{R}$ the pressure difference $\Delta\hat{p}$ becomes negative for some $\hat{h}$. The height of the standard catenoid (distance between the two frames, Fig. S10a) is

$$h_1 = 2a \ \operatorname{arccosh}(R/a). \tag{S23}$$

The volume of the standard catenoid (volume between one frame and the mid plane with $z = 0$, see Fig. S10a) is

$$V_1 = \int_0^{h_1/2} \pi r^2 \mathrm{d}z = \pi a^2 \left(\frac{h_1}{2} + \frac{a}{2}\sinh\frac{h_1}{a}\right). \tag{S24}$$

A diabolo catenoid is obtained by subtracting the red part from the grey part in Fig. S10a. The red part depends on θ_c, obtained with eqn. (S22) and given with

$$h_2 = 2a \ \operatorname{arcsinh}(\cot(\theta_c)). \tag{S25}$$

The volume V_2 of the red part is obtained with the eqn. (S24) by replacing h_1 with h_2. The volume of a diabolo catenoid (bottom of Fig. S10a) is then simply

$$V = V_1 - V_2. \tag{S26}$$

The distance between the two frames is

$$h = h_1 - h_2. \tag{S27}$$

As the neck a is always smaller than R, the ratio $a/R < 1$. Therefore, a similar procedure as in Section. S2.2 is used with $0 < a/R < 1$ instead of $\tilde{F}_{z;\min} \leq \tilde{F}_z \leq \tilde{F}_{z;\max}$. One obtains all possible catenoid solutions for a given θ_c. By normalising R, h and a with eqn. (14) with the volume V from eqn. (S26), we obtain $\hat{R}$ and $\hat{h}$. Fig. S10b shows this dependency of the smallest $\hat{R}$ on θ_c with $\Delta\hat{p} = 0$. For larger $\hat{R}$ there are always two catenoid solutions with different $\hat{h}$ and different $\hat{a}$.

S5 Surface Evolver

Converged surfaces in Surface Evolver are always in an energy minimum. The energy gradient is in this case zero. By making a Taylor expansion around this minimum one obtains information about the second derivative the Hessian matrix $\underline{H}$, eqn. (S28)

$$E(\vec{v}_0 + d\vec{v}_0) = E_0 + \nabla E \cdot d\vec{v}_0 + \frac{1}{2} d\vec{v}_0 \vec{v}_0{}^T \cdot \underline{H} \cdot d\vec{v}_0 \tag{S28}$$

The vector $\vec{v}_0$ represents the coordinates of all vertices of the Surface Evolver model in the converged state. The surface energy is E. Since we consider here only converged surfaces, $\nabla E(\vec{v}_0) = 0$ and the change in E depends locally only on $\underline{H}$. The eigenvalues of the Hessian matrix λ_i are always positive, if the energy is in a minimum. A shape transition is related to an eigenvalue which approaches zero. For the extremum to be stable, all eigenvalues of $\underline{H}$ must be positive.

S6 Tilt instability CB↔TB

The point for the tilting instability is obtained experimentally and with Surface Evolver. Fig. S11 shows the evolution of the two smallest eigenvalues of the Hessian matrix with respect to the frame distance $\hat{h}$.

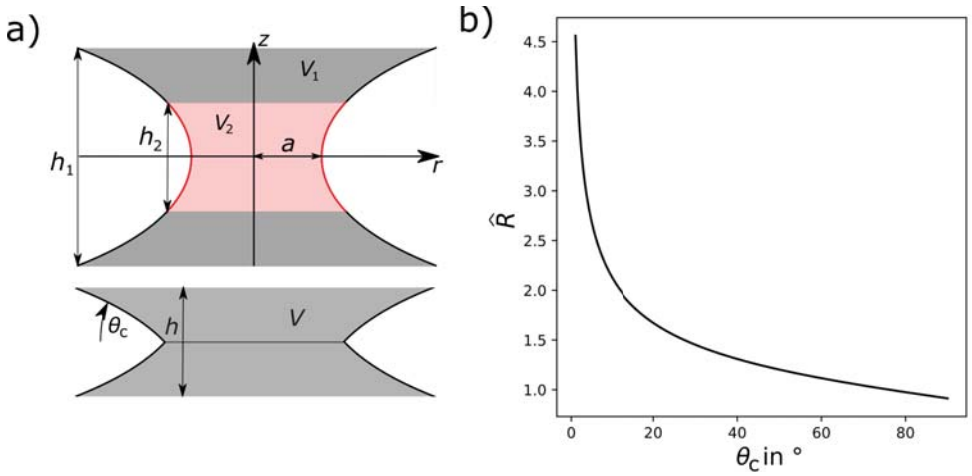

Figure S10: a) An illustration of the standard catenoid (top) and a diabolo catenoid (bottom) with the important geometrical parameters, explained in the text. b) The smallest $\hat{R}$ where the surface is a part of a catenoid as a function of the contact angle θ_c.

For a specific height the smallest eigenvalue λ_0 and second smallest λ_1 decrease rapidly and reach almost zero in comparison to other eigenvalues. Afterwards λ_0 stays almost zero and λ_1 increases rapidly again. λ_0 is not perfectly zero due to the precision of Surface Evolver. The two eigenvalues are equal if the surface is axissymetric. The point where $\lambda_0 \neq \lambda_1$ is the point of instability for the tilting instability. The reason why λ_0 stays zero (in Surface Evolver $\lambda_0 \approx 0$) is because the surface can rotate around the z-axis without energy change. The tilted state is therefore a Goldstone mode. The reason why the plateau in Fig. S11 where $\lambda_0 \approx 0$ is not the same is because λ_i is proportional to the number of facets in the Surface evolver model.

The precision of the tilting/shifting point in Surface Evolver can be estimated with help of a convergence study. Fig. S12 shows that the critical height $\hat{h}_{CB\leftrightarrow TB}$, where the surface looses the axisymmetry, converges against a value for increasing number of facets. We worked with approximately 5000-10000 facets, which gives us a precision of approximately 0.1%.

The contact surface of the tilted bubbles is shown in Fig. S13 for two different θ_c. It has to be a minimal surface since the pressure difference between the two bubbles is zero. However the surface is not a plane anymore, as can be seen in Fig. S13. We define a new coordinate system with (x', y', z') where $\vec{e}_{z'}$ is normal to the best fitting plane of the contact surface. That defines the tilting angle φ with:

$$\cos(\varphi) = \vec{e}_z \cdot \vec{e}_{z'} \tag{S29}$$

Note the different scaling for the z' axis, needed to reveal the small changes in z' compared to x' and y' extension. The difference to a tilted plane is not detectable experimentally. The three ridges and three valleys change in amplitude by changing $\hat{h}$. The angle φ can be used as an order parameter to investigate the shape transition from the axisymmetric configuration to the tilted configuration.

In Fig. 9, the force only changes its slope at the critical point $\hat{h}_{CB\leftrightarrow TB}$. We do not see any force jump, which suggests that this shape transition is a second order shape transition. Noting that the energy of the system is a function of the angle φ with a periodicity of π, we use a Landau approach, the total energy of the system is described with $\sin(\varphi)$

$$E = E_0(\varphi = 0) + a(\hat{h})\sin(\varphi)^2 + b(\hat{h})\sin(\varphi)^4 \tag{S30}$$

Close to a second order shape transition, we can make the approximation $a(h) = a_0(h - \hat{h}_{CB\leftrightarrow TB})$ and $b(\hat{h}) = b_0$. For $\hat{h} < \hat{h}_{CB\leftrightarrow TB}$ one obtains two minima with the equation

$$\sin(\varphi)^2 = -\frac{a_0}{b_0}\left(\hat{h} - \hat{h}_{CB\leftrightarrow TB}\right). \tag{S31}$$

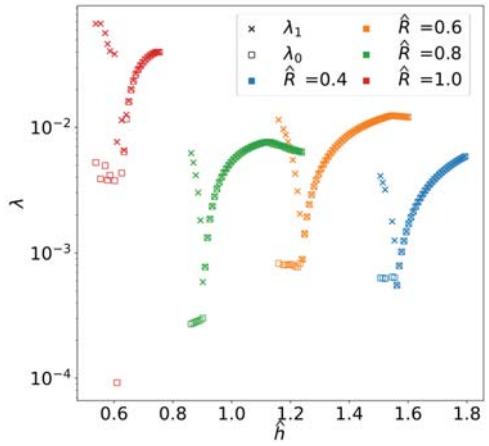

Figure S11: The two smallest eigenvalues λ_i of the Hessian matrix obtained with Surface evolver for different $\hat{R}$ plotted over the frame distance $\hat{h}$.

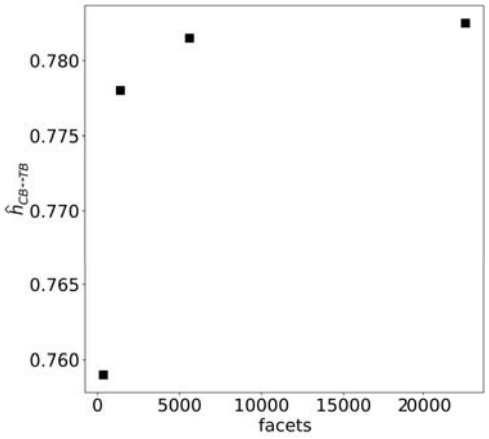

Figure S12: Height $\hat{h}_{CB\leftrightarrow TB}$ where the surface looses the axisymmetry for a simulation in Surface Evolver with different number of facets ([352, 1408, 5632, 22528]), $\hat{R} = 0.4$ and $\theta_c = 60°$.

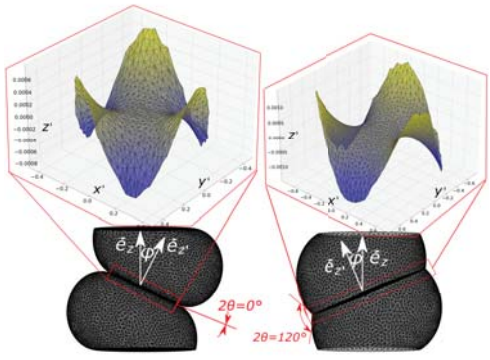

Figure S13: Examples of tilted bubble configurations simulated in Surface Evolver. Left: $\theta_c = 0°$. Right: $\theta_c = 60°$. The upper part of the figure shows the shape of the contact film in the (x',y',z') coordinate system which has been rotated by φ.

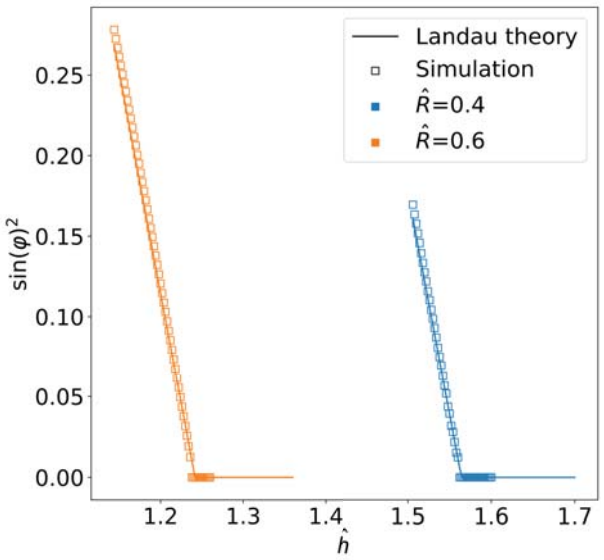

Figure S14: Comparison between the tilt angle $\sin(\varphi)^2$ obtained with the Surface Evolver simulations and with the eqn.s (S31) and (S32) for two different $\hat{R}$.

For $\hat{h} > \hat{h}_{CB\leftrightarrow TB}$ one obtains one minimum with the equation

$$\varphi^2 = 0. \tag{S32}$$

Since only energy minima give stable shapes, we use eqn. (S32) for $\hat{h} > \hat{h}_{CB\leftrightarrow TB}$ and use eqn. (S31) for $\hat{h} < \hat{h}_{CB\leftrightarrow TB}$. In Fig. S14 we compare the theory from eqn. (S31) and the simulated φ. $\hat{h}_{CB\leftrightarrow TB}$ and a_0/b_0 are obtained by fitting φ from the simulation. The difference between the fitted $\hat{h}_{CB\leftrightarrow TB}$ and the $\hat{h}_{CB\leftrightarrow TB}$ obtained with help of the eigenvalues is below 0.3%. Which is also close to the precision of the simulation. This Landau approach can be extended to describe the tilted film shape and even the shape of the shifted bubbles (ShB). Further information can be found in the thesis of Friedrich Walzel [9].

S7 Delaunay Surfaces without mirror symmetry

There are stable Delaunay Surfaces which are not mirror symmetric to the xy-mid plane - but only if the upper and lower frame radius are not identical. Since in experiments that is always the case due to inaccuracies and rim thicknesses, we observed some of them in our experiments. An example is shown in Fig. S15.

Figure S15: A Delaunay Surfaces obtained with a capillary bridge, which is not mirror symmetric to the xy-min plane.

References

[1] K.L. Mittal. *Advances in Contact Angle, Wettability and Adhesion, Volume 2*. Adhesion and Adhesives: Fundamental and Applied Aspects. Wiley, 2015.

[2] Caroline Cohen, Baptiste Darbois Texier, Etienne Reyssat, Jacco H Snoeijer, David Quéré, and Christophe Clanet. On the shape of giant soap bubbles. *Proceedings of the National Academy of Sciences*, 114(10):2515–2519, 2017.

[3] Bhagya Athukorallage, Thanuja Paragoda, and Magdalena Toda. Roulettes of conics, delaunay surfaces and applications. *Surveys in Mathematics and Mathematical Sciences*, 4(1):1–20, 2014.

[4] Wikipedia. Conic sections, 2023.

[5] RD Gillette and DC Dyson. Stability of fluid interfaces of revolution between equal solid circular plates. *The Chemical Engineering Journal*, 2(1):44–54, 1971.

[6] Thomas I Vogel. Stability of a liquid drop trapped between two parallel planes. *SIAM Journal on Applied Mathematics*, 47(3):516–525, 1987.

[7] John H Maddocks. Stability and folds. *Archive for Rational mechanics and Analysis*, 99:301–328, 1987.

[8] Louis Salkin, Alexandre Schmit, Pascal Panizza, and Laurent Courbin. Influence of boundary conditions on the existence and stability of minimal surfaces of revolution made of soap films. *American Journal of Physics*, 82(9):839–847, 2014.

[9] Friedrich Walzel. *From interacting bubbles and drops to soft capsules: shape, mechanics and stability analysis*. PhD thesis, Université de Strasbourg, 2024.